An Interaction Algorithm for Three-Dimensional Turbulent Subsonic Aerodynamic Juncture Region Flow

A. J. Baker*
University of Tennessee, Knoxville, Tennessee
and
J. A. Orzechowski†
Computational Mechanics Consultants, Inc., Knoxville, Tennessee

An order-of-magnitude analysis of the subsonic three-dimensional, steady time-averaged Navier-Stokes equations for semibounded aerodynamic juncture geometries yields the parabolic Navier-Stokes simplification. The numerical solution of the resultant pressure Poisson equation is cast into complementary and particular parts, yielding an iterative interaction algorithm with an exterior three-dimensional potential flow solution. A parabolic transverse momentum equation set is constructed, wherein robust enforcement of first-order continuity effects is accomplished using a penalty differential constraint concept within a finite-element solution algorithm. A Reynolds stress constitutive equation, with low-turbulence Reynolds number wall functions, is employed for closure, using parabolic forms of the two-equation turbulent kinetic energy-dissipation equation system. The algorithm is employed to predict the three-dimensional turbulent flowfield in the juncture region formed by two intersecting parabolic arcs at $M_\infty = 0.08$ and $Re/C = 0.6 \times 10^6$/m. Additional results document the turbulence closure model.

Introduction

A PRINCIPAL requirement in aerodynamics is flow prediction in juncture regions formed by the intersection of aerodynamic surfaces, e.g., wing-body, wing-winglet, pylon-wing, etc. In most instances of interest, the associated flow is three-dimensional, subsonic with variable density, and turbulent. A characteristic action of such flows is vortex roll-up in the plane transverse to the chord coordinate, and mass efflux/influx into the boundary-layer regions located at some distance from the juncture region. The principal requirements of a juncture region flow analysis are to predict the vortex structure, hence to yield a corner drag coefficient, and to provide transverse plane velocity boundary conditions for a conventional three-dimensional boundary-layer solution of the associated far-field flow.

The essential aspects of the problem are illustrated in the geometry of the idealized exterior subsonic axial corner, see Fig. 1, which has received considerable theoretical and experimental attention. Rubin et al.[1-4] pioneered in formulation and analysis of the three-dimensional laminar corner flow problem. Tokuda[5] documents an extension of this analysis and a comparison of prediction to the experimental data of Zamir and Young.[6] Bragg[7] analyzed the corresponding turublent flow case and determined the corner distribution of the chordwise Reynolds normal stress component $\overline{u_i' u_j'}$. The salient feature of the turbulent flow case is inducement of a persistent axial vorticity component. Various causal mechanisms have been theorized, including transverse pressure waves,[8] Reynolds shear stress gradients along the corner bisector,[9] and nonisotropy of the Reynolds stress tensor.[10] Quality experimental data for a confined corner flow[11] compared to computational results confirm the primary mechanisms to be nonisotropy of the Reynolds stress tensor $\overline{u_i' u_j'}$.

The character in the idealized corner region flow thus appears to be the result of a delicate balance between the turbulence phenomena and the induced secondary mean flow velocity field. However, these mechanisms represent a balancing of higher order effects, as discussed herein, and can be readily dominated by the vorticity induced by flowfield curvature.[12,13] Nevertheless, an adequate Reynolds stress closure model is required and has been developed for this problem class. The six components of the (symmetric) Reynolds stress tensor are determined using a tensor field constitutive equation formulation which requires solution of parabolized forms of the transport equations for turbulent kinetic energy k and isotropic dissipation function ϵ. The stress constitutive equation includes a low-turbulence Reynolds number length scale model to permit solution of the (k,ϵ) equation system directly through the sublayer region adjacent to an aerodynamic surface. Hence, the boundary conditions for the k and ϵ solutions are identically vanishing at all aerodynamic surfaces.

A pressure-velocity formulation is preferred to predict turbulent aerodynamic junction region flows. While definition of a transverse plane potential function[14] can automatically satisfy the continuity equation, the elimination of transverse pressure gradients comes at the expense of definition and use of vorticity. The acknowledged weakness of the vorticity formulation is the kinematic boundary condition statement. The existence of large mean flow strain rates at an aerodynamic surface, for turbulent flow, serve to further complicate this intrinsic weakness. The physical variables formulation does not encounter this problem, but instead a rearrangement of equation form is required. An order-of-magnitude analysis indicates that pressure distributions will balance convection and/or turbulence effects to first order, and that overall this balance is of higher order effects than those controlled by the continuity equation. Since the continuity equation is not parabolic for subsonic flow, the construction of a suitable transverse plane equation system is required.

The pressure-velocity formulation is derived and evaluated herein for steady turbulent flow prediction in three-dimensional, semibounded aerodynamic juncture region domains. Persistence of the chordwise component of the time-

Presented as Paper 82-0100 at the AIAA 20th Aerospace Sciences Meeting, Orlando, Fla., Jan. 11-14, 1982; submitted Jan. 25, 1982; revision received July 19, 1982.

*Professor, Engineering Science and Mechanics. Associate Fellow AIAA.

†Principal Consultant.

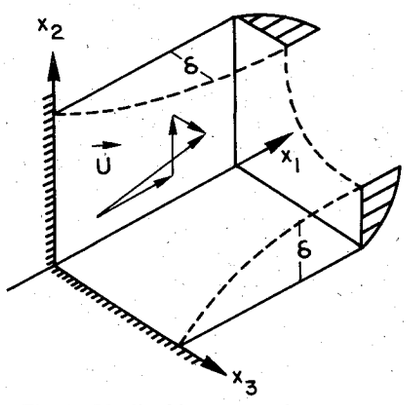

Fig. 1 Idealized juncture region geometry.

averaged, mean flow velocity permits an order-of-magnitude analysis, yielding the parabolic approximation to the governing three-dimensional, steady time-averaged Navier Stokes equations. Using the same procedure for components of the Reynolds stress tensor, the balancing of lowest order terms in the two transverse momentum equations yields a pressure Poisson equation. An algorithm for this equation is derived in terms of complementary and particular solution fields. The complementary solution is determined using boundary conditions obtained from an exterior potential flow solution. The particular solution refines this pressure determination by accounting for the Reynolds stress and transverse velocity distributions. The particular solution is enforced in a retarded manner in the chordwise momentum equation pressure field. Algorithm convergence occurs when this composite pressure solution becomes stationary. As a consequence of the ordering analysis, the number of dependent variables requiring solution exceeds the available equations. Therefore, using finite-element penalty function concepts in constrained extremization, cf. Oden,[15] a transverse momentum equation solution statement is constructed wherein the first-order effects of the nonparabolic continuity equation are enforced as a differential constraint.

Problem Description

Parabolic Navier-Stokes Equations

The three-dimensional parabolic Navier-Stokes (3DPNS) equations are a simplification of the steady, three-dimensional time-averaged Navier-Stokes equations. In Cartesian tensor notation, and employing superscript tilde and bar to denote mass-weighted[16] and conventional time-averaging, the conservative equation form is

$$L(\bar{\rho}) = \frac{\partial}{\partial x_j}[\bar{\rho}\tilde{u}_j] = 0 \tag{1}$$

$$L(\bar{\rho}\tilde{u}_i) = \frac{\partial}{\partial x_j}[\bar{\rho}\tilde{u}_i\tilde{u}_j + \bar{p}\delta_{ij} + \bar{\rho}\overline{u_i'u_j'} - \bar{\sigma}_{ij}] = 0 \tag{2}$$

$$L(\bar{\rho}\tilde{H}) = \frac{\partial}{\partial x_j}[\bar{\rho}\tilde{H}\tilde{u}_j - \tilde{u}_i\bar{\sigma}_{ij} + \bar{\rho}\overline{H'u_j'} - \overline{u_i'\sigma_{ij}'} + \bar{q}_j] = 0 \tag{3}$$

$$L(\bar{\rho}k) = \frac{\partial}{\partial x_j}\left[\bar{\rho}\tilde{u}_j k + \left(C_k\frac{k}{\epsilon}\bar{\rho}\overline{u_i'u_j'} - \bar{\mu}\delta_{ij}\right)\frac{\partial k}{\partial x_i}\right] + \bar{\rho}\overline{u_i'u_j'}\frac{\partial \tilde{u}_i}{\partial x_j} + \bar{\rho}\epsilon = 0 \tag{4}$$

$$L(\bar{\rho}\epsilon) = \frac{\partial}{\partial x_j}\left[\bar{\rho}\tilde{u}_j\epsilon + C_\epsilon\frac{k}{\epsilon}\bar{\rho}\overline{u_i'u_j'}\frac{\partial \epsilon}{\partial x_i}\right] + C_\epsilon'\bar{\rho}\overline{u_i'u_j'}\frac{\epsilon}{k}\frac{\partial \tilde{u}_i}{\partial x_j} + C_\epsilon^2\frac{\bar{\rho}\epsilon^2}{k} = 0 \tag{5}$$

In Eqs. (1-3), $\bar{\rho}$ is density, $\tilde{u}_j$ the mean velocity vector, $\bar{p}$ the pressure, δ_{ij} the Kronecker delta, and $\tilde{H}$ the stagnation enthalpy. The Stokes stress tensor $\bar{\sigma}_{ij}$ and heat flux vector $\bar{q}_j$ are defined as,

$$\bar{\sigma}_{ij} = \bar{\rho}\bar{\nu}(\bar{E}_{ij} - \tfrac{2}{3}\delta_{ij}\bar{E}_{kk})/Re \tag{6}$$

$$\bar{q}_j = \kappa\frac{\partial \tilde{H}}{\partial x_j} \tag{7}$$

where Re is the reference Reynolds number, $Re = U_\infty L/\nu_\infty$, and $-\bar{\rho}\overline{u_i'u_j'}$ is the Reynolds stress tensor. In Eqs. (6) and (7), $\bar{\nu}$ and $\bar{\kappa}$ are the fluid kinematic viscosity and heat conductivity, respectively, and $\bar{E}_{ij}$ is the mean flow strain rate tensor

$$\bar{E}_{ij} = \frac{\partial \tilde{u}_i}{\partial x_j} + \frac{\partial \tilde{u}_j}{\partial x_i} \tag{8}$$

Equations (4) and (5) are the transport equations for turbulent kinetic energy and isotropic dissipation function, using the closure model of Launder, Reece, and Rodi[17] for the pressure-strain and triple correlations, and

$$k \equiv \tfrac{1}{2}\overline{u_i'u_i'} \tag{9}$$

$$\epsilon \equiv \frac{2\bar{\nu}}{3}\overline{\left[\frac{\partial u_i'}{\partial x_j}\frac{\partial u_i'}{\partial x_k}\right]}\delta_{jk} \tag{10}$$

The various coefficients C_β^α are model constants.[18]

The parabolic Navier-Stokes equation set is derived from Eqs. (1-5) by assuming the ratio of transverse mean velocity components to chordwise components is less than unity, and by further assuming that:

1) The chordwise velocity component suffers no reversal.

2) Diffusive transport processes in the chordwise direction are of higher order and hence negligible.

3) The overall elliptic character of the parent three-dimensional Navier-Stokes equations is enforceable through construction of a suitable pressure field with exterior flow boundary conditions.

Assume the x_1 (curvilinear) coordinate direction parallel to the chordwise mean flow direction, with scalar velocity component $\tilde{u}_1$ of order unity, i.e., 0(1). Further assume $0(\tilde{u}_2) \approx 0(\delta) \approx 0(\tilde{u}_3)$, and that $0(\delta) < 0(1)$. In agreement with boundary-layer theory, Eq. (1) confirms the order of chordwise variation in $\tilde{u}_1$ and appropriate transverse variation of $\tilde{u}_2$ and $\tilde{u}_3$ is equal, i.e., for

$$\frac{\partial}{\partial x_1} \approx 0(1), \quad \frac{\partial}{\partial x_2} \approx 0(\delta^{-1}) \approx \frac{\partial}{\partial x_3}$$

Determination of the relative order of terms for $i = 1$ in the momentum equation (2) is straightforward. Since $0(\bar{\rho}\overline{u_1'u_j'})$ must be $0(\delta)$, the term $\partial/\partial x_1(\bar{\rho}\overline{u_i'u_j'})$ is higher order and can be discarded. The assumption that the x_1 – diffusion is negligible permits setting $\partial/\partial x_1(\bar{E}_{11}) \equiv 0$, hence $0(Re)^{-1} \leq 0(\delta)$. Therefore, the terms in $\bar{\sigma}_{12}$ and $\bar{\sigma}_{13}$ involving $\tilde{u}_2$ and $\tilde{u}_3$, i.e.,

$$\frac{\partial}{\partial x_2}\left(\frac{\partial \tilde{u}_2}{\partial x_1}\right) \text{ and } \frac{\partial}{\partial x_3}\left(\frac{\partial \tilde{u}_3}{\partial x_1}\right)$$

are both $0(\delta)$ or smaller and negligible. Deletion of these terms is the fundamental step to the parabolic approximation, since their elimination removes the elliptic boundary value character in the chordwise direction.

Since the term $(\partial/\partial x_1)(\bar{\rho}\tilde{u}_1\tilde{u}_1)$ remains, it instills an initial value character for the resultant equation which permits

marching the solution for $\tilde{u}_1$ in the chordwise direction. The resultant 3DPNS form, dentoed $L^p(\cdot)$, is therefore,

$$L^p(\bar{\rho}\tilde{u}_1) \equiv \frac{\partial}{\partial x_j}(\bar{\rho}\tilde{u}_j\tilde{u}_1) + \frac{\partial \bar{p}}{\partial x_1} + \frac{\partial}{\partial x_2}[\bar{\rho}\overline{u_1'u_2'} - \bar{\sigma}_{12}] + \frac{\partial}{\partial x_3}[\bar{\rho}\overline{u_1'u_3'} - \bar{\sigma}_{13}] = 0 \tag{11}$$

which is thoroughly familiar. Should x_j correspond to a curvilinear coordinate description, the derivatives expressed in Eq. (11) are interpreted as covariant. The 3DPNS form for the energy equation (3) is,

$$L^p(\bar{\rho}H) = \frac{\partial}{\partial x_1}(\bar{\rho}\tilde{u}_1\tilde{H}) + \frac{\partial}{\partial x_\ell}[\bar{\rho}\tilde{H}\tilde{u}_\ell - \tilde{u}_i\bar{\sigma}_{i\ell} + \bar{\rho}\overline{H'u_\ell'} - \overline{u_i'\sigma_{i\ell}'} + \bar{q}_\ell] = 0 \tag{12}$$

which introduces the 3DPNS limited index summation convention $1 \le i \le 3$ and $2 \le \ell \le 3$.

In agreement with boundary-layer concepts, the order of pressure variation in the transverse plane is determined by the lowest order terms appearing in Eq. (2) for $i=2,3$. Each transverse derivative of $\bar{\rho}\overline{u_2'u_j'}$ and $\bar{\rho}\overline{u_3'u_j'}$ is 0(1), while all other terms are $0(\delta)$ and higher. For a conventional two-dimensional boundary-layer flow then, for example,

$$L(\bar{\rho}\tilde{u}_2) \approx \frac{\partial}{\partial x_2}[\bar{p} + \bar{\rho}\overline{u_2'u_2'}] = 0 \tag{13}$$

The solution is trivial; $\bar{p}$ differs from the inviscid flow edge pressure by a constant equal to a fraction of the freestream turbulence k level, and is distributed through the boundary layer in proportion to $\bar{\rho}\overline{u_2'u_2'}$. The initial value character for pressure, as exhibited by the 3DPNS first-order approximation to Eq. (2) for $i=2,3$, is rendered numerically tractible by taking the divergence. Retaining the higher order convection and diffusion terms for generality, the 3DPNS form for both transverse momentum equations is

$$L(\bar{p}) = \frac{\partial^2 \bar{p}}{\partial x_\ell^2} + \frac{\partial^2}{\partial x_j \partial x_\ell}[\bar{\rho}\tilde{u}_\ell\tilde{u}_j + \bar{\rho}\overline{u_\ell'u_j'} - \bar{\sigma}_{tj}] = 0 \tag{14}$$

Equation (14) is an elliptic boundary value problem definition for pressure distribution in the transverse plane with parametric dependence on x_1. The pressure that satisfies this quasilinear Poisson equation consists of complementary and particular solutions, i.e.,

$$\bar{p}(x_i) = p_c(x_i) + p_p(x_i) \tag{15}$$

The complementary solution satisfies the homogeneous form of Eq. (14),

$$L(p_c) = \frac{\partial^2 p_c}{\partial x_\ell^2} = 0 \tag{16}$$

The Dirichlet boundary condition for Eq. (16) is $p_c(x_1,\tilde{x}_\ell) \equiv \bar{p}(x_1,\tilde{x}_\ell)$ on the intersection of the 3DPNS domain with the exterior potential flow domain. Elsewhere, the boundary condition for p_c is homogeneous Neumann.

The particular pressure is any solution to Eq. (14) subject to homogeneous Dirichlet boundary conditions on boundary segments where p_c is known. Elsewhere, the nonhomogeneous Neumann constraint is provided by the inner product of the 3DPNS form of Eq. (2), written on $\tilde{u}_\ell$, with the local outward pointing unit normal $\hat{\eta}_\ell$,

$$\ell(p_p) \equiv L^p(\bar{\rho}\tilde{u}_\ell)\cdot\hat{\eta}_\ell = \frac{\partial}{\partial x_\ell}[p_p + \rho\overline{u_\ell'u_\ell'}] + \frac{\partial}{\partial x_k}[\rho\overline{u_k'u_\ell'}] = 0 \tag{17}$$

Repeated indices in Eq. (17) are not summed, and $k=2,3$ for $k \neq \ell$. Hence, Eq. (17) is the generalization of the boundary-layer form [Eq. (13)]. Following determination of the order of terms in the Reynolds stress tensor in the next section, the nonhomogeneous terms in Eq. (17) vanish to the lowest order on an aerodynamic surface. Thereupon $p_p(x_1,\tilde{x}_\ell)$ is a constant which is zero. Elsewhere on the 3DPNS domain boundary, Eq. (17) yields the appropriate boundary condition for Eq. (14).

Reynolds Stress Tensor Closure

Closure for the kinematic Reynolds stress tensor $-\overline{u_i'u_j'}$ appearing in Eqs. (4) and (5) is required to complete the 3DPNS order-of-magnitude analysis. The necessary insight is provided by construction of a tensor field strain rate constitutive equation, cf., Ref. 19, the existence of which is assured at "sufficient" distance from boundaries in space and time.[20] Using lower dimensional order-of-magnitude analyses and invariance, the three lead terms of the five-term kinematic expansion are

$$-\overline{u_i'u_j'} = -k\alpha_{ij} + C_4\frac{k^2}{\epsilon}\bar{E}_{ij} + C_2C_4\frac{k^3}{\epsilon^2}\bar{E}_{ik}\bar{E}_{kj} + \ldots \tag{18}$$

where $\bar{E}_{ij}$ is the symmetric mean flow strain rate tensor [Eq. (8)], k and ϵ the turbulence parameters defined in Eq. (9) and (10), and α_{ij} the diagonal tensor in principal coordinates,

$$\alpha_{ij} \equiv \frac{1}{3k}(\overline{u_k'u_k'})a_i\delta_{ij} \tag{19}$$

The a_i are coefficients admitting anisotropy, and $a_i \equiv C_1$, and $a_2 \equiv C_3 \equiv a_3$, where the C_α $(1 \le \alpha \le 4)$ are constants, algebraically related to two "universal" empirical constants.[18]

The order of terms in Eq. (18) can be estimated for the standard values, $C_\alpha = \{0.94, 0.067, 0.56, 0.068\}$. For a two-

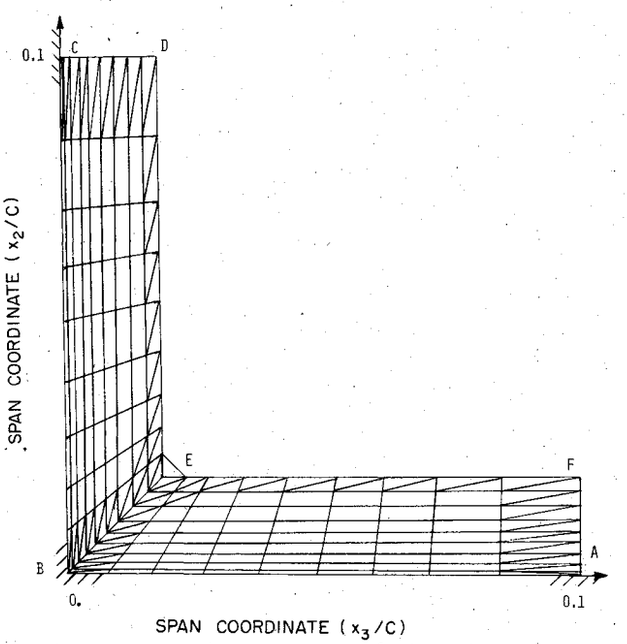

Fig. 2 Finite-element discretization of R^2 for the 3DPNS solution.

dimensional flow, and for $i=1$ and $j=2$, Eq. (18) yields the familiar form [of $0(\delta)$],

$$-\overline{u_1'u_2'} = C_4 \frac{k^2}{\epsilon} \frac{\partial \tilde{u}_1}{\partial x_2} \tag{20}$$

Hence, $0(C_4k^2/\epsilon)=0(\delta^2)$. Further for $i=1=j$ in Eq. (18), and neglecting the second two terms, $0(k)=0(\delta)$, hence $0(C_4/\epsilon)=0(1)=0(C_2/\epsilon)$. Thus, $0[C_2C_4(k^3/\epsilon^2)]\approx 0(\delta^3)$.

Therefore, in rectangular Cartesian coordinates, and retaining terms of the first two orders of significance, the six components of the kinematic Reynolds stress tensor are

$$\begin{aligned}
\overline{u_1'u_1'} &= C_1k - C_2C_4\frac{k^3}{\epsilon^2}\left[\left(\frac{\partial \tilde{u}_1}{\partial x_2}\right)^2+\left(\frac{\partial \tilde{u}_1}{\partial x_3}\right)^2\right] && -2C_4\frac{k^2}{\epsilon}\left[\frac{\partial \tilde{u}_1}{\partial x_1}\right] \\
\overline{u_2'u_2'} &= C_3k - C_2C_4\frac{k^3}{\epsilon^2}\left[\frac{\partial \tilde{u}_1}{\partial x_2}\right]^2 && -2C_4\frac{k^2}{\epsilon}\left[\frac{\partial \tilde{u}_2}{\partial x_2}\right] \\
\overline{u_3'u_3'} &= C_3k - C_2C_4\frac{k^3}{\epsilon^2}\left[\frac{\partial \tilde{u}_1}{\partial x_3}\right]^2 && -2C_4\frac{k^2}{\epsilon}\left[\frac{\partial \tilde{u}_3}{\partial x_3}\right] \\
\overline{u_1'u_2'} &= -C_4\frac{k^2}{\epsilon}\left[\frac{\partial \tilde{u}_1}{\partial x_2}\right] && -C_2C_4\frac{k^3}{\epsilon^2}\left[\frac{\partial \tilde{u}_1}{\partial x_3}\left(\frac{\partial \tilde{u}_2}{\partial x_3}+\frac{\partial \tilde{u}_3}{\partial x_2}\right)+2\frac{\partial \tilde{u}_1}{\partial x_2}\left(\frac{\partial \tilde{u}_1}{\partial x_1}+\frac{\partial \tilde{u}_2}{\partial x_2}\right)\right] \\
\overline{u_1'u_3'} &= -C_4\frac{k^2}{\epsilon}\left[\frac{\partial \tilde{u}_1}{\partial x_3}\right] && -C_2C_4\frac{k^3}{\epsilon^2}\left[\frac{\partial \tilde{u}_1}{\partial x_2}\left(\frac{\partial \tilde{u}_2}{\partial x_3}+\frac{\partial \tilde{u}_3}{\partial x_2}\right)+2\frac{\partial \tilde{u}_1}{\partial x_3}\left(\frac{\partial \tilde{u}_1}{\partial x_1}+\frac{\partial \tilde{u}_3}{\partial x_3}\right)\right] \\
\overline{u_2'u_3'} &= -C_2C_4\frac{k^3}{\epsilon^2}\left[\frac{\partial \tilde{u}_1}{\partial x_2}\frac{\partial \tilde{u}_1}{\partial x_3}\right] && -C_4\frac{k^2}{\epsilon}\left[\frac{\partial \tilde{u}_2}{\partial x_3}+\frac{\partial \tilde{u}_3}{\partial x_2}\right]
\end{aligned} \tag{21}$$

($0(\delta)$ terms / $0(\delta^2)$ terms)

Two conclusions regarding Eq. (21) should be noted. The terms which provide an elliptic boundary value definition for the direct integration of Eq. (2) for $\tilde{u}_2$ and $\tilde{u}_3$ are indeed $0(\delta^2)$, in agreement with the ordering arguments leading to Eq. (14). Second, the $0(\delta)$ term in $-\overline{u_2'u_3'}$ in Eq. (21) vanishes on an aerodynamic surface, hence p_p is a constant. The order of terms in Eqs. (4) and (5) can thus be determined, yielding the 3DPNS approximations as

$$L^p(k) = \frac{\partial}{\partial x_i}(\bar{\rho}\tilde{u}_i k) + \frac{\partial}{\partial x_i}\left[\bar{\rho}\left(C_k\frac{k}{\epsilon}\overline{u_i'u_\ell'} - \bar{\nu}\delta_{i\ell}\right)\frac{\partial k}{\partial x_\ell}\right] + \bar{\rho}\overline{u_i'u_\ell'}\frac{\partial \tilde{u}_1}{\partial x_\ell} + \bar{\rho}\epsilon = 0 \tag{22}$$

$$L^p(\epsilon) = \frac{\partial}{\partial x_i}(\rho\tilde{u}_i\epsilon) + \frac{\partial}{\partial x_i}\left[\bar{\rho}C_\epsilon\frac{k}{\epsilon}\overline{u_i'u_\ell'}\frac{\partial \epsilon}{\partial x_\ell}\right] \times C_\epsilon^1\bar{\rho}\overline{u_i'u_\ell'}\frac{\epsilon}{k}\frac{\partial \tilde{u}_1}{\partial x_\ell} + C_\epsilon^2\bar{\rho}\frac{\epsilon^2}{k} = 0 \tag{23}$$

Definition of boundary conditions for Eqs. (22) and (23) addresses the issue of what constitutes "sufficient" distance for the validity of Eq. (18). For two-dimensional flows, one approach is to employ similarity arguments to assign values to k and ϵ at some distance from the wall, e.g., $10<y^+<50$, where $y^+ \equiv u_\tau x_2/\bar{\nu}$ is a turbulence Reynolds number based on the wall shear velocity,[16] $u_\tau \equiv \sqrt{\tau_w/\bar{\rho}}$. Extension of this concept to three-dimensional flows is questionable, but has been attempted.[21] A second alternative suggests modifying the "constants" C_β^α appearing in Eqs. (22) and (23) and integrating directly through the low-turbulence wall region with $k\equiv 0\equiv\epsilon$ as boundary conditions.

A third alternative approach[23] is employed for the juncture region analysis. The "constants" C_α of the Reynolds stress constitutive equation (18) are modified to account for low turbulence levels in the sublayer region. Equation (20) defines the conventional turbulent "eddy viscosity," $\nu^t \equiv C_4k^2/\epsilon$. Using dimensional analysis, ν^t is the product of a scale velocity with a scale length; typically, for a turbulence kinetic energy model,

$$\nu^t \equiv k^{1/2}\ell_d \tag{24}$$

Comparison with Eq. (20) yields the familiar relationship

$$\ell_d \equiv C_4k^{3/2}/\epsilon \tag{25}$$

Recalling the van Driest damping function ω, defined to control evolution of the Prandtl mixing length scale,[16] Eq. (25) multiplied by ω yields Eq. (20) in the form

$$-\overline{u_1'u_2'} = \omega C_4\frac{k^2}{\epsilon}\frac{\partial \tilde{u}_1}{\partial x_2} \tag{26}$$

The van Driest form for ω is modified for variable length scale damping as

$$\omega \equiv [1-\exp(-by^+/A^+)] \tag{27}$$

where $A^+\approx 26$, and $b\approx 2.0$ based upon results of numerical studies.[23,24] Premultiplying each coefficient C_α in Eq. (18) by ω produces the required modification. Furthermore, C_ϵ^2 in Eq. (23) is also multiplied by ω. The aerodynamic surface boundary conditions for Eqs. (22) and (23) are then $k\equiv 0\equiv\epsilon$.

Differential Equation System Closure

The consistently ordered 3DPNS system [Eqs. (11), (12), (14), (18), (22), and (23)] numbers one less than the number of dependent variables defined in Eqs. (1-10). Therefore, at least one equation governing $0(\delta)$ phenomena must be included to close the system. Since the 3DPNS momentum equation (11) is written on $\tilde{u}_1$ only, both components of $\tilde{u}_\ell \equiv \{\tilde{u}_2, \tilde{u}_3\}$ are required determined subject to the constraint of continuity [Eq. (1)]. The finite-element algorithm ac-

complishes this by "penalizing" the solution of the $0(\delta)$ 3DPNS approximation to the momentum equation (2), written on each component of u_ℓ, by the continuity equation. Retaining the first two orders of terms, the 3DPNS form for the transverse momentum equations is

$$L^p(\bar{\rho}\tilde{u}_k) = \frac{\partial}{\partial x_1}[\bar{\rho}\tilde{u}_1\tilde{u}_k + \bar{\rho}\overline{u_1'u_k'}] + \frac{\partial}{\partial x_\ell}[\bar{\rho}\tilde{u}_\ell\tilde{u}_k + \bar{\rho}\overline{u_\ell'u_k'} + \bar{p}\delta_{k\ell} - \bar{\sigma}_{k\ell}] = 0 \tag{28}$$

which introduces the additional 3DPNS limited index $2 \le k \le 3$. The middle two terms in the second bracket are $0(\delta)$, while the remaining terms are all $0(\delta^2)$ or smaller. Equation (28) exhibits elliptic boundary value character upon retaining the terms of $0(\delta^2)$ in the Reynolds stress tensor equation (18) and contains the initial value term permitting chordwise marching.

Since Eq. (28) represents two additional scalar equations, an auxiliary dependent variable is required. The theoretical concept, borrowed from the variational calculus, is to define a suitable measure of the continuity equation (solution error), which becomes a differential constraint on solution of the transverse plane momentum equation (28). The constraint measure must span R^2 and vanish as the continuity equation becomes satisfied. One appropriate variable is the harmonic function $\phi(x_\ell)$, the solution to the Poisson equation,

$$L^p(\phi) \equiv \frac{\partial^2\phi}{\partial x_\ell^2} - \frac{\partial}{\partial x_i}(\bar{\rho}\tilde{u}_i) \equiv 0 \tag{29}$$

subject to homogeneous Neumann conditions on portions of the domain boundary ∂R, and setting $\phi = 0$ at one location at least on ∂R. Equation (29) becomes homogeneous, when the continuity equation is identically satisfied, and the solution $\phi(x_\ell)$ becomes null as a consequence of the boundary condition specifications.

Finite Element Solution Algorithm

The consistently ordered 3DPNS equation system is identified for the dependent variable set $q_\alpha(x_i) \equiv \{q\} = \{\bar{\rho}, \tilde{u}_1, \tilde{u}_2, \tilde{u}_3, \tilde{H}, \bar{p}, k, \epsilon, -\overline{u_i'u_j'}, \phi\}^T$. An equation of state $\bar{\rho} = \bar{\rho}(\bar{p}, H)$ closes the system. Equations (11), (12), (22), (23), and (28) contain the initial value term that facilitates the solution marching in the chordwise direction. Equations (14) and (29) are elliptic boundary value descriptions with parametric initial value dependence, while Eq. (18) is algebraic. Equation (1) becomes recast as the differential constraint using Eq. (29).

Therefore, the general 3DPNS description is,

$$L^p(q_\alpha) = \frac{\partial}{\partial x_1}(\bar{\rho}\tilde{u}_1 q_\alpha) + \frac{\partial}{\partial x_\ell}[\bar{\rho}\tilde{u}_\ell q_\alpha + g_{\ell\alpha}] + s_\alpha = 0 \tag{30}$$

where $g_{\ell\alpha}$ and s_α are specified nonlinear functions of their arguments, as determined by the index α. The solution domain Ω is the product of R^2 and x_1 for all elements of x_1 belonging to the open interval measured from $x_1(0)$, i.e.,

$$\Omega \equiv R^2 \times x_1 = \{(x_\ell, x_1):\ x_\ell \epsilon R^2 \text{ and } x_1 \epsilon [x_1(0), x_1]\}$$

The boundary of the solution domain is the product of the boundary ∂R or R^2 and x_i, i.e., $\partial\Omega \equiv \partial R \times x_1$. Thereupon, a differential constraint is applied of the form,

$$\ell(q_\alpha) = a_1^\alpha q_\alpha + a_2^\alpha \frac{\partial}{\partial x_i} q_\alpha \hat{\eta}_i + a_3^\alpha = 0 \tag{31}$$

where the a_i^α are specified and $\hat{\eta}_i$ is the outward pointing unit normal vector. Finally, an initial distribution for the appropriate members of q_j on $\Omega_0 \equiv R^2 \times x_1(0)$ is required,

$$q_j(x_\ell, x_1(0)) \equiv q_j^0(x_\ell) \tag{32}$$

For the finite-element numerical solution algorithm of Eqs. (30) and (31), the approximation $q_\alpha^h(x_\ell, x_1)$ to the (unknown) exact solution $q_\alpha(x_\ell, x_1)$ is constructed from members of a finite-dimensional subspace of $H_0^1(\Omega)$, the Hilbert space of all functions possessing square integrable first derivatives and satisfying the boundary conditions. While extremely flexible in theory, the practice for the 3DPNS equation system is to employ linear polynomials defined on disjoint interior triangular-shaped subdomains R_e^2, the union of which forms the discretization of R^2. Hence, the finite-element approximation is,

$$q_\alpha(x_\ell, x_1) \approx q_\alpha^h(x_\ell, x_1) \equiv \sum_{e=1}^{M} q_\alpha^e(x_\ell, x_1) \tag{33}$$

using the elemental construction,

$$q_\alpha^e(x_\ell, x_1) \equiv \{N_I(x_\ell)\}^T \{QJ(x_1)\}_e \tag{34}$$

where J is the discrete free index denoting members of q_α^h at nodes of $\cup R_e^2$, and sub- or superscript e denotes pertaining to the eth finite-element, $\Omega_e \equiv R_e^2 \times x_1$. The elements of the row matrix $\{N_I(x_\ell)\}^T$ are linear polynomials on x_ℓ constructed to form a cardinal basis.[25]

The functional requirement of any numerical solution algorithm is to extremize the semidiscrete approximation error in q_α^h in some norm. The finite-element algorithm requires that the error in Eqs. (30) and (31), i.e., $L^p(q_\alpha^h)$ and $\ell(q_\alpha^h)$, be orthogonal to the space $\{N_k(x_\ell)\}$ employed to define q_α^h. In addition, the discrete approximation $L^p(\bar{\rho}^h)$ to the continuity equation (1) must be enforced as a differential constraint. Identifying the (Lagrange) multiplier set as β_i, these linearly independent constraints are combined to yield the finite-element solution algorithm theoretical statement,

$$\int_{R^2} \{N_k\} L^p(q_\alpha^h)\,d\mathbf{x} + \beta_1 \int_{\partial R} \{N_k\} \ell(q_\alpha^h)\,d\mathbf{x} + \beta_2 \int_{R^2} \nabla\{N_k\} L^p(\bar{\rho}^h)\,d\mathbf{x} \equiv \{0\} \tag{35}$$

Equation (35) is a system of ordinary differential equations, written on the chordwise coordinate x_1, of the form

$$[C]\{QJ\}' + [U]\{QJ\} + \{GJ\} + \{SJ\} = \{0\} \tag{36}$$

An accurate and efficient integration algorithm for Eq. (36) is the trapezoidal rule. Hence,

$$\{FJ\} \equiv \{QJ\}_{j+1} - \{QJ\}_j - \frac{\Delta x_1}{2}[\{QJ\}'_{j+1} + \{QJ\}'_j] \equiv \{0\} \tag{37}$$

defines a system of nonlinear algebraic equations for determination of the elements of $\{QJ(x_1)\}$. Substituting Eq. (36), the Newton algorithm for Eq. (37) is

$$[J(FJ)]^p_{j+1}\{\delta QJ\}^{p+1}_{j+1} = -\{FJ\}^p_{j+1} \tag{38}$$

The dependent variable is the iteration vector, related to the solution $\{QJ\}$ in the conventional manner,

$$\{QJ\}^{p+1}_{j+1} = \{QJ\}^p_{j+1} + \{\delta QJ\}^{p+1}_{j+1} \tag{39}$$

Additional details on the algorithm construction are given in Ref. 26.

Table 1 3DPNS boundary condition specifications aerodynamic juncture region

Dependent variables	Boundary segment	Boundary conditions[31] a_1	a_2	a_3
$\tilde{u}_1$, $\tilde{u}_\ell$, k, ϵ, p_p	ABC	1	0	0
	CDEFA	0	1	0
p_c	DEF	1	0	$\tilde{p}$
	FABCD	0	1	0
ϕ	DEF	1	0	0
	FABCD	0	1	0

For the $k=1$ basis embodiment of the 3DPNS algorithm [Eq. (35)] a linearized truncation error analysis indicates second-order spatial accuracy. The trapezoidal rule for integration is also second-order accurate. The 3DPNS equations contain the two-dimensional boundary-layer system as a subset and Soliman and Baker[27,28] document the pertinent accuracy and convergence data for $k=1,2$, and for laminar and turbulent flow.

Results and Discussion

The test case is turbulent flow in the aerodynamic juncture region formed by the right interaction of two 10% thick parabolic arcs with coincident leading edges. Figure 1 illustrates the essential geometry and Fig. 2 graphs the nonuniform $M=325$ discretization of the transverse plane R^2 as the union of the triangles (with diagonals omitted for clarity). The domain boundary ∂R is the union of straight-line segments A-F, upon which boundary conditions are required (see Table 1).

The complimentary pressure p_c boundary conditions were obtained using the Hess code[29] for $M_\infty=0.08(U_\infty=30$ m/s ≈ 100 f/s) and zero angle of attack. Figure 3 summarizes the span distributions of $p_c(\bar{x}_\ell)$ at chord stations $x_1/C=0.01$, 0.085, and 0.46. By symmetry, these also occur at $x_1/C=0.54$, 0.915, and 0.99. Therefore, the favorable x_1 pressure gradient decreases uniformly to midchord and thereafter turns progressively adverse. The strongest gradients occur in the immediate corner vicinity, i.e., $x_\ell/C<0.2$.

The unit Reynolds number is $Re/C=0.6\times10^6$/m and the flow is assumed isoenergetic, hence $\tilde{H}(x_i)=$ const. The initial conditions for $u_1^0(x_\ell)$ at the nodes of R^2 are established using Cole's law[16] to interpolate a turbulent boundary layer onto node "columns" (Fig. 2), with the matching of the freestream level of $p_c(\bar{x})$. The transverse velocity $\tilde{u}_\ell$ is defined as identically zero until eight 3DPNS steps are completed, to permit computation of an acceptable chordwise derivative of $\bar{\rho}\tilde{u}_1$, i.e., $\{RHOU1\}'$. The initial distributions of $k^\circ(x_\ell)$ and $\epsilon^\circ(x_\ell)$ are computed using mixing length boundary-layer concepts.[23,28]

During the 3DPNS solution, the particular pressure solution $p_p(x_\ell,x_1)$ is written on the output file at each chord station x_1 for which $p_c(\bar{x}_\ell,x_1)$ boundary conditions are specified. For the second and sequential 3DPNS solutions, the solution of Eq. (16) is algebraically summed with the previously stored distributions $p_p(x_\ell,x_1)$ for the chordwise pressure gradient distribution in the $\tilde{u}_1$ momentum equation solution. The $\tilde{u}_\ell$ momentum equations are solved using the current computed p_p distributions. The composite pressure field $\bar{p}(x_i)/p_0$ converges to five significant digits following three 3DPNS algorithm solutions for the parabolic arc juncture region. The nominal level of p_p/p_0 is 10^{-3}; a representative extremum difference between the second and third 3DPNS solutions is $\Delta p_p/p_0\approx10^{-5}$ at $x_1/C=0.17$.

The 3DPNS solution for the defined juncture region flow is exactly mirror symmetric. Figure 4 summarizes the third-interaction 3DPNS solution evolution of the lower surface distribution of $\tilde{u}_\ell(x_\ell,x_1)$ on $0.021\le x_1/C\le0.7$. A massive

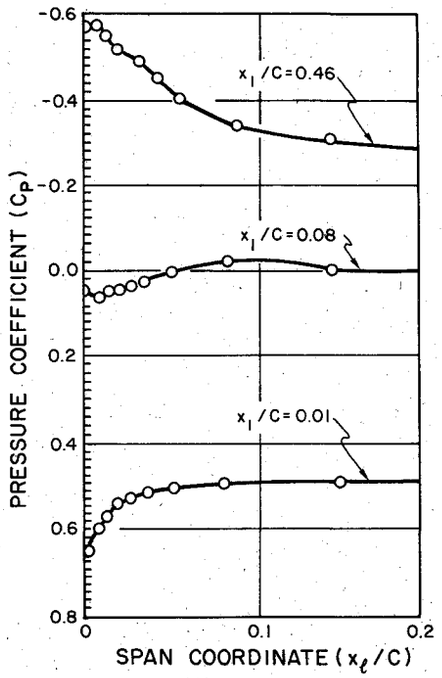

Fig. 3 Three-dimensional potential flow boundary conditions for complementary pressure.

influx into the corner region is predicted at $x_1/C=0.021$, with the extremum scalar component $\tilde{u}_\ell^m/\tilde{u}_1=0.167$, i.e., equal to 17% of the local freestream value of $\tilde{u}_1$. This is the direct result of the associated large favorable pressure gradient of $\tilde{u}_1$, coupled with the fact that the mass conservation algorithm has just become initialized. By $x_1/C=0.047$, the extremum scalar component is $\tilde{u}_\ell^m/\tilde{u}_1=0.072$ and the juncture blockage is inducing a large spanwise efflux from R^2 in the lower reaches of the boundary layer. A corner axial vortex (pair) is just visible at $x_1/C=0.081$, where the minimum level of $\tilde{u}_\ell$ is predicted. This transverse plane velocity distribution changes only nominally to well beyond midchord, with $\tilde{u}_\ell^m/\tilde{u}_1\approx10\%$ throughout. The generated corner vortex pair persists and the spanwise efflux fills the entire boundary layer. Past midchord, the freestream velocity derivative changes sign, with a concurrent cessation of influx from the potential region.

Figure 5 compares the third-interaction 3DPNS transverse plane velocity distribution at $x_1/C=0.46$ for laminar and turbulent flow solutions. In comparison, the corner vortex pair is slightly larger for laminar flow, the extremum component $\tilde{u}_\ell^m/\tilde{u}_1=0.06$ is 40% smaller in magnitude, and reversed spanwise flow is predicted in the lowest reach of the far-field boundary layer (Fig. 5a). Shafir and Rubin[30] predict this lower reach reversal for laminar/turbulent boundary-layer transition. Further, the flowfield in Fig. 5a is in qualitative agreement with the composite corner-layer/asymptotic boundary-layer solution reported by Rubin and Grossman.[3]

Figure 6 is a summary of transverse plane isoclines of $\tilde{u}_1$ and components of $\overline{u_i'u_j'}$ at $x_1/C=0.46$, for the third-interaction 3DPNS solution. The $\tilde{u}_1$ solution exhibits the intrinsic symmetry with a modest relative displacement directly adjacent to the corner, the result of the axial vortex pumping low-momentum fluid into the corner and out parallel to the diagonal. The plot of $\overline{u_1'u_1'}$ is also symmetric and a local extrema exists in the corner due to the axial vortex. These comments are appropriate for $\overline{u_2'u_2'}$, except that this normal stress exhibits a (very) modest nonsymmetry due to the $0(\delta^2)$ term involving $\tilde{u}_1$ in Eq. (21). The $\overline{u_1'u_2'}$ shear stress distribution is highly nonsymmetric, with the extremum level penetrating only half the span distance to the corner. On the upper

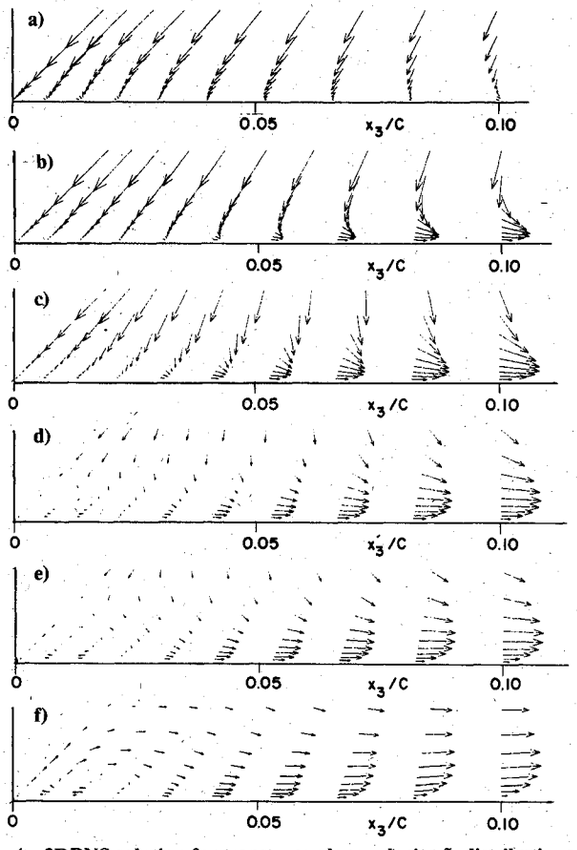

Fig. 4 3DPNS solution for transverse plane velocity $\tilde{u}_\ell$ distributions, turbulent parabolic arc junction region flow: a) $x_1/C=0.021$, $\tilde{u}_\ell^m/\tilde{u}_1=0.167$; b) $x_1/C=0.047$, $\tilde{u}_\ell^m/\tilde{u}_1=0.072$; c) $x_1/C=0.081$, $\tilde{u}_\ell^m/\tilde{u}_1=0.058$; d) $x_1/C=0.173$, $\tilde{u}_\ell^m/\tilde{u}_1=0.112$; e) $x_1/C=0.349$, $\tilde{u}_\ell^m/\tilde{u}_1=0.114$; f) $x_1/C=0.704$, $\tilde{u}_\ell^m/\tilde{u}_1=0.097$.

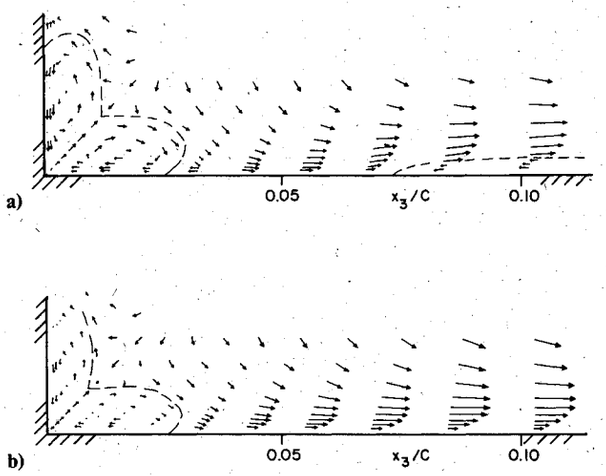

Fig. 5 3DPNS solution for transverse plane velocity $\tilde{u}_\ell$ distributions, juncture region flow, $x_1/C=0.46$: a) laminar flow, $\tilde{u}_\ell^m/\tilde{u}_1=0.06$; b) turbulent flow, $\tilde{u}_\ell^m/\tilde{u}_1=0.10$.

half domain, these levels are very small, since $\tilde{u}_1(x_\ell)$ is a weak function of x_2 along the vertical span. Of course, $\overline{u_1'u_3'}$ is a mirror reflection of $\overline{u_1'u_2'}$.

No complete experimental data exist for quantitative comparison of the juncture region turbulent flow 3DPNS prediction. However, such a data set exists[11] for turbulent flow in a straight, uniform rectangular cross-sectional duct. Following localized entrance region effects, experiments verify that no consequential transverse plane velocities exist far downstream for laminar flow. Conversely, for turbulent

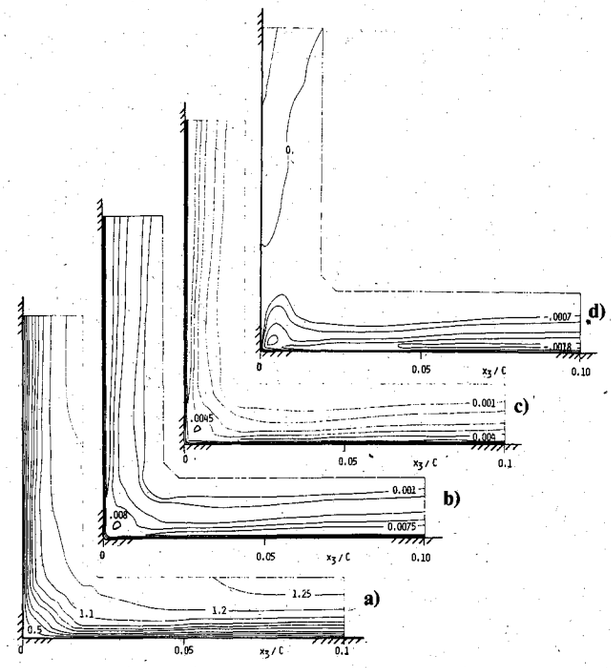

Fig. 6 3DPNS solution summary, parabolic arc juncture region flow, turbulent, $Re/C=6.0\times10^5$, $M_\infty=0.08$, $x_1/C=0.46$: a) $\tilde{u}_1$, b) $\overline{u_1'u_1'}$, c) $\overline{u_2'u_2'}$, d) $\overline{u_1'u_2'}$.

flow four persistent axial vortex pairs are created, one in each right-angle corner of the duct. Baker and Orzechowski[31] document qualitative agreement with these observations for the 3DPNS solution on a coarse ($M=288$) discretization of the symmetric quarter duct. Specifically, no vortex pair roll-up occured for laminar flow or for the turbulent flow prediction with the $0(\delta)$ terms involving $\tilde{u}_1$ derivatives in $\overline{u_\ell'u_\ell'}$ set to zero, see Eq. (21). However, with these terms included, as theoretically required by invariance, the turbulent flow 3DPNS prediction immediately generated the corner vortex pair.

Refined grid and full-duct solutions for the experimental configuration have been computed. Figure 7a shows the experimental data for the transverse plane velocity distribution $\tilde{u}_\ell(x_1=37, x_\ell)$, with $\tilde{u}_\ell^m/\tilde{u}_1=0.0086$. Figure 7b is the refined ($M=1052$) grid solution on the symmetric quarter duct. The qualitatively correct vortex patterns nearly fill the section, and $\tilde{u}_\ell^m/\tilde{u}_1=0.0043$ is only a factor of two lower than the data. Small but erroneous vortices are predicted adjacent to both symmetry planes, but their size is substantialy reduced in comparison to the coarse grid solution.[31] The $M=288$ and 1052 results confirm that the mechanism causing this local pollution of the solution is a singularity in the boundary conditions for the conservation function $\phi^h(x_\ell)$. Since a velocity component is permitted (must occur) parallel to the symmetry plane, but not along the no-slip wall, the corner intersection corresponds to a discontinuous switch from Dirichlet to Neumann boundary conditions.

The 3DPNS solution on a coarse ($M=1052$) grid discretization of the entire duct did predict extinction of the spurious vortices. However, this grid is too coarse for quantitative assessments. The quarter-duct $M=1052$ 3DPNS solution is of appropriate refinement, and the pollution due to the singularity is rather localized. Admitting these limitations, Figs. 8-11 compare the experimental data[11] with the $M=1052$ 3DPNS solution. Figure 8 verifies significant instrusion of the high-momentum core velocity $\tilde{u}_1$ into the corner region, as induced by the vortex structure (Fig. 7). The intersection of the 3DPNS $\tilde{u}_1=0.70$ isovel with the symmetry plane is in good agreement with experiment. Above this level, and on the symmetry planes, the intersection of 3DPNS levels for $\tilde{u}_1$

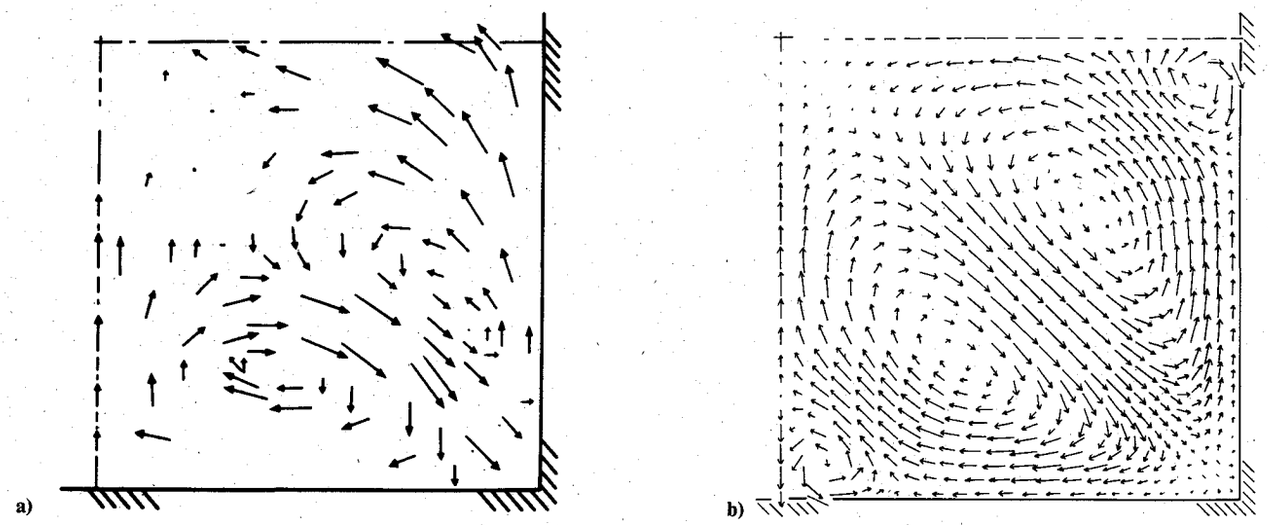

Fig. 7 3DPNS and experimental distributions of transverse plane velocity $\tilde{u}_\ell$, turbulent rectangular duct flow: a) experimental,[11] $\tilde{u}_\ell^m/\tilde{u}_1 = 0.0086$; b) 3DPNS solution, $M = 1052$, $\tilde{u}_\ell^m/\tilde{u}_1 = 0.0043$.

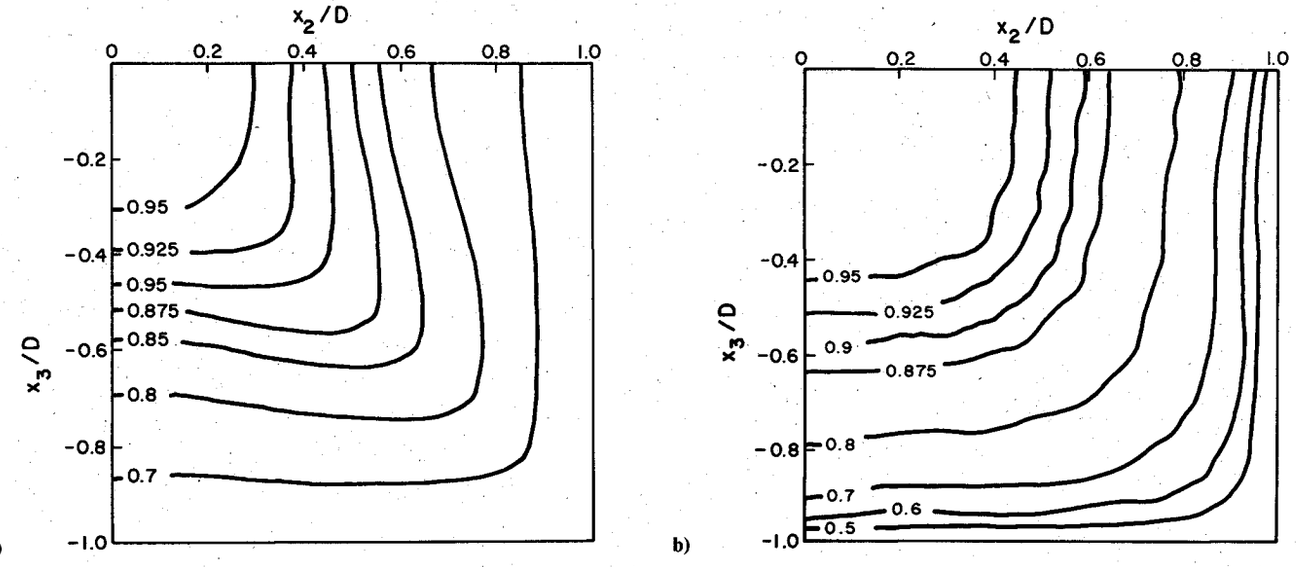

Fig. 8 3DPNS and experimental distributions of mean velocity $\tilde{u}_1$, turbulent rectangular duct flow: a) experimental,[11] $x_1/D = 37.0$, b) 3DPNS solution, $x_1/D = 35.8$.

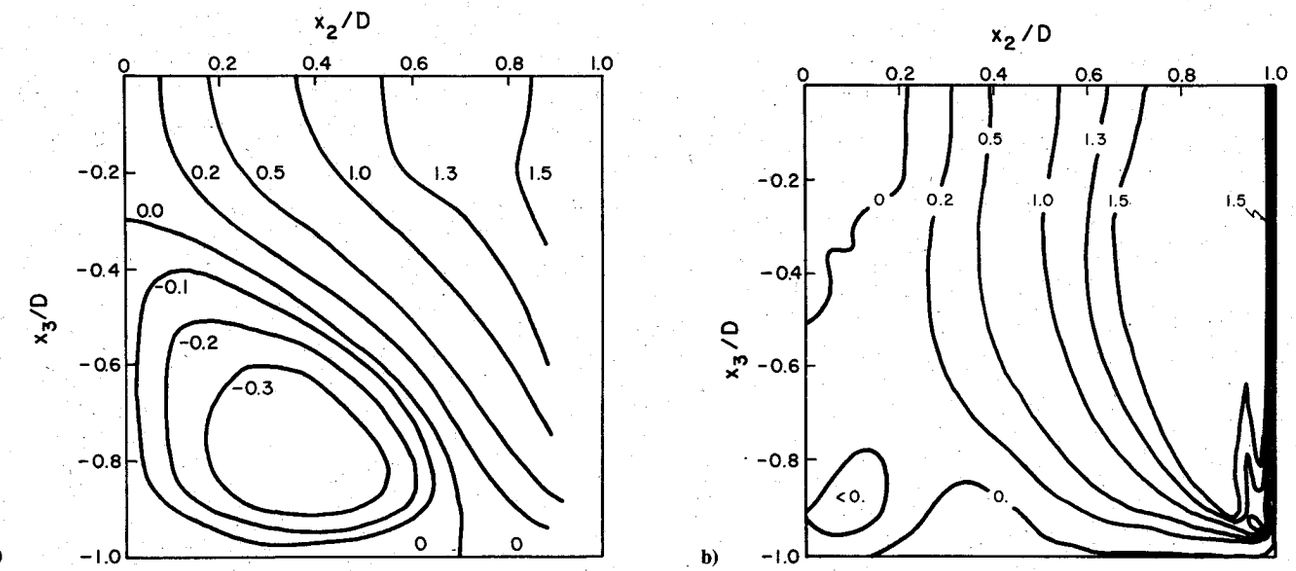

Fig. 9 3DPNS and experimental distributions, Reynolds shear stress $-u_1'u_2' \times 10^4$, turbulent rectangular duct flow: a) experimental,[11] $x_1/D = 37.0$; b) 3DPNS solution, $x_1/D = 35.8$.

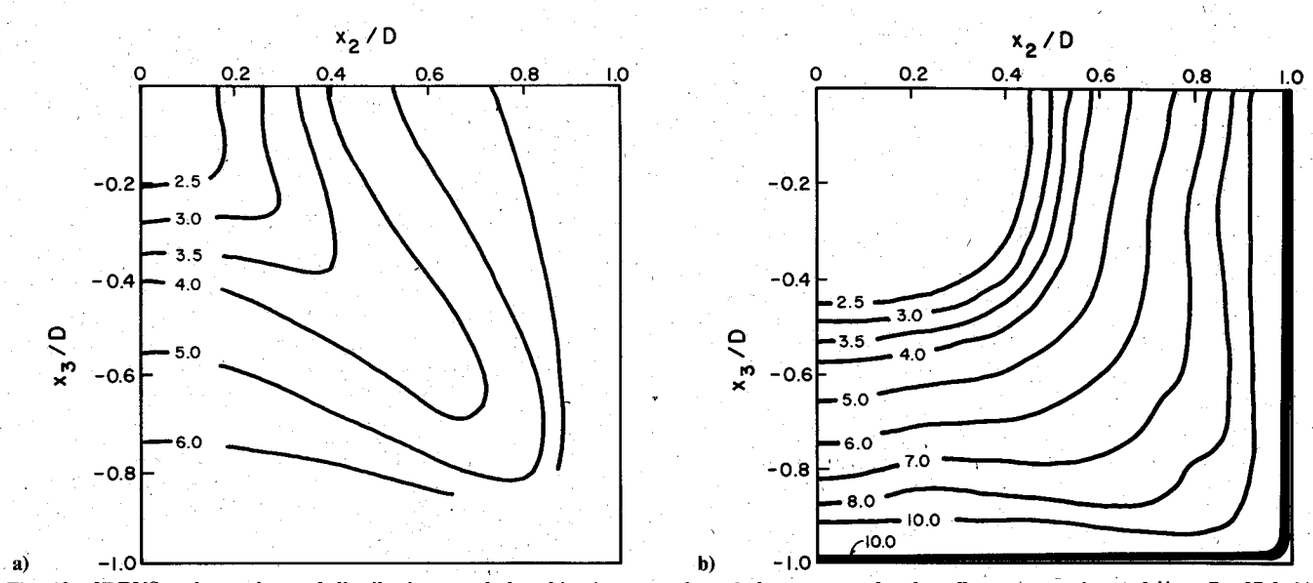

Fig. 10 3DPNS and experimental distributions, turbulent kinetic energy k, turbulent rectangular duct flow: a) experimental,[11] $x_1/D=37.0$; b) 3DPNS solution, $x_1/D=35.8$.

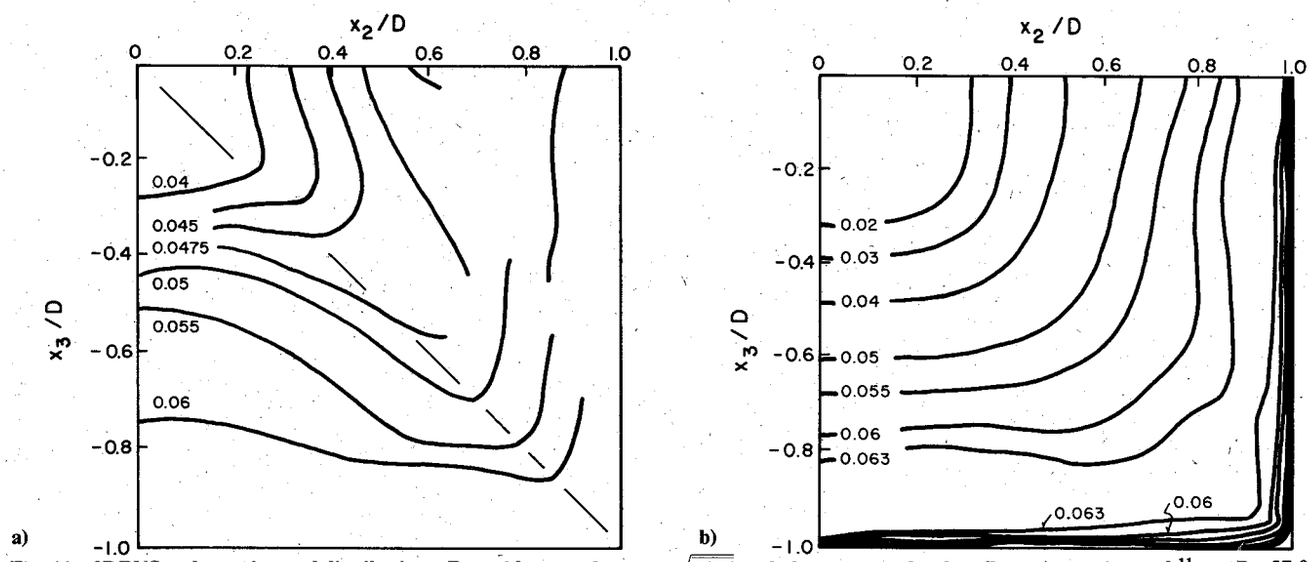

Fig. 11 3DPNS and experimental distributions, Reynolds normal stress $-\sqrt{\overline{u_2'u_2'}}$ turbulent rectangular duct flow: a) experimental,[11] $x_1/D=37.0$; b) 3DPNS solution, $x_1/D=35.8$.

exceeds data by $\Delta x_\ell \approx 15\%$. Along the corner bisector, the levels are in better agreement.

Figure 9 compares the Reynolds $\overline{u_1'u_2'}$ shear stress distributions. Good overall agreement on level is indicated, as well as some detail of the contour shapes for the largest levels. The experimentally measured regions of small negative $u_1'u_2'$ (and small positive $u_1'u_3'$) shear stress result from the inflections in $\bar{u}_1$ (Fig. 8). The 3DPNS solution has correctly predicted this essential character, although the details are largely affected by the boundary-condition singularity effects.

Figures 10 and 11 compare components of the Reynolds normal stresses. The overall agreement on levels confirms the standard definitions for the constitutive equation model constants C_α [Eq. (21)] and the coefficients C_α^β in Eqs. (22) and (23). The 3DPNS prediction for k is symmetric (Fig. 10b), in agreement with the data, but the intrusion of the core region levels along the domain bisector is consequentially underpredicted. The intersection of $k=0.075$ on the symmetry plane is in good agreement, and the higher solution levels exhibit better agreement with data. The intersection of $k=0.05$ is different by $\Delta x_\ell \approx 20\%$, indicating the level of turbulence in the experimental core flow is considerably larger than that of the 3DPNS simulation. Figure 11 compares the transverse plane normal stress $\sqrt{\overline{u_2'u_2'}}$. Agreement on overall levels is good, with the 3DPNS prediction exhibiting the essential nonsymmetries of the data. The 3DPNS solution for $\sqrt{\overline{u_3'u_3'}}$ is exactly mirror symmetric with $\sqrt{\overline{u_2'u_2'}}$. These (modest) nonsymmetries are computationally confirmed to be the principal causal mechanism of the counter-rotating vortex structure.

Summary

An order-of-magnitude analysis has yielded a consistent physical variables formulation for the parabolic approximation to the three-dimensional Navier-Stokes equations for steady, turbulent subsonic flow. A finite-element numerical solution algorithm is established using a penalty differential constraint statement. A tensor field expansion is employed to provide closure for the Reynolds stress distribution, in concert with solution of two turbulent transport equations. A composite pressure field construction is identified to enforce overall ellipticity, using a multipass interaction solution procedure with a three-dimensional potential flow exterior solution. Numerical results document the robustness of the key elements of the developed algorithm for the aerodynamic juncture region geometry.

Acknowledgments

This work was principally supported by the NASA Langley Research Center under NASA Contract NAS1-15105. The authors wish to acknowledge the considerable computer support provided by the University of Tennessee Computer Center during the computer program development phase.

References

[1] Rubin, S. G., "Incompressible Flow Along a Corner," *Journal of Fluid Mechanics,* Vol. 26, Pt. 1, 1966, pp. 97-110.

[2] Pal, A. and Rubin, S. G., "Asympototic Features of Viscous Flow Along a Corner," *Quarterly of Applied Mathematics,* Vol. 27, 1971, pp. 99-108.

[3] Rubin, S. G. and Grossman, B., "Viscous Flow Along a Corner: Numerical Solution of the Corner Layer Equations," *Quarterly of Applied Mathematics,* Vol. 29, No. 2, 1971, pp. 169-186.

[4] Weinberg, B. C., and Rubin, S. G., "Compressible Corner Flow," *Journal of Fluid Mechanics,* Vol. 56, Pt. 4, 1972, pp. 753-774.

[5] Tokuda, N., "Viscous Flow Near a Corner in Three Dimensions, *Journal of Fluid Mechanics,* Vol. 53, Pt. 1, 1972, pp. 129-148.

[6] Zamir, M. and Young, A. D., "Experimental Investigation of the Boundary Layer in a Streamwise Corner," *Aeronautical Quarterly,* Vol. 21, 1970, pp. 313-339.

[7] Bragg, G. M., "The Turbulent Boundary Layer in a Corner," *Journal of Fluid Mechanics,* Vol. 36, Pt. 3, 1969, pp. 485-503.

[8] Eichelbrenner, E. A. and Preston, J. H., "On a Role of Secondary Flow in Turbulent Boundary Layers in Corners (and Salients)," *Journal de Mechanique,* Vol. 10, No. 1, 1971, pp. 91-112.

[9] Gessner, F. B., "The Origin of Secondary Flow in Turbulent Flow Along a Corner," *Journal of Fluid Mechanics,* Vol. 58, Pt. 1, 1973, pp. 1-25.

[10] Gessner, F. B. and Emery, A. F., "A Reynolds Stress Model for Turbulent Corner Flows—Pt. I: Development of the Model," *Journal of Fluids Engineering, Transactions of ASME,* 1976, pp. 261-268.

[11] Melling, A. and Whitelaw, J. H., "Turbulent Flow in a Rectangular Duct," *Journal of Fluid Mechanics,* Vol. 78, Pt. 2, 1976, pp. 289-315.

[12] Shabaka, I. M. M. A. and Bradshaw, P., "Turbulent Flow Measurement in an Idealized Wing/Body Juncture," *AIAA Journal,* Vol. 19, Feb. 1981, pp. 131-132.

[13] McMahon, H., Hubbartt, J., and Kubendran, L., "Mean Velocities and Reynolds Stress in a Juncture Flow," NASA Tech. Rept. CR-3605, 1982.

[14] Briley, W. R. and McDonald, H., "Analysis and Computation of Viscous Subsonic Primary and Secondary Flows," AIAA Paper 79-1453, 1979.

[15] Oden, J. T., "A Theory of Penalty Methods for Finite Element Approximations of Highly Nonlinear Problems in Continuum Mechanics," *Computers and Structures,* Vol. 8, 1978, pp. 445-449.

[16] Cebeci, T. and Smith, A. M. O., *Analysis of Turbulent Boundary Layers,* Academic Press, New York, 1974.

[17] Launder, B. E., Reece, G. J., and Rodi, W., "Progress in the Development of a Reynolds-Stress Turbulence Closure," *Journal of Fluid Mechanics,* Vol. 3, Pt. 3, 1975, pp. 537-566.

[18] Hanjalic, K. and Launder, B. E., "A Reynolds Stress Model of Turbulence and Its Application to Thin Shear Flows," *Journal of Fluid Mechanics,* Vol. 52, Pt. 4, 1972, pp. 609-638.

[19] Daly, B. J. and Harlow, F. H., "Transport Equations in Turbulence," *Physics of Fluids,* Vol. 13, No. 11, 1970, pp. 2634-2649.

[20] Lumley, J. L., "Toward a Turbulent Constitutive Relation," *Journal of Fluid Mechanics,* Vol. 41, Pt. 2, 1970, pp. 413-434.

[21] Pratap, V. S. and Spalding, D. B., "Numerical Computations of the Flow in Curved Ducts," *Aeronautical Quarterly,* Vol. 26, 1975.

[22] Rodi, W., "Examples of Turbulence Models for Incompressible Flows," *AIAA Journal,* Vol. 20, July 1982, pp. 872-879.

[23] Baker, A. J., Yu, J. C., Orzechowski, J. A., and Gatski, T. B., "Prediction and Measurement of Incompressible Turbulent Aerodynamic Trailing Edge Flows," *AIAA Journal,* Vol. 20, Jan. 1982, pp. 51-59.

[24] Baker, A. J. and Orzechowski, J. A., "An Interaction Algorithm for Prediction of Mean and Fluctuating Velocities in Two-Dimensional Aerodynamic Wake Flows," NASA CR-3301, 1980.

[25] Prenter, P. M., *Splines and Variational Methods,* Wiley-Interscience, New York, 1975.

[26] Baker, A. J., "The CMC: 3DPNS Computer Program for Prediction of Three-Dimensional, Subsonic, Turbulent Aerodynamic Juncture Flow, Vol. I: Theoretical," NASA Tech. Rept., 1982.

[27] Soliman, M. O. and Baker, A. J., "Accuracy and Convergence of a Finite Element Algorithm for Laminar Boundary Layer Flow," *Journal of Computers and Fluids,* Vol. 9, 1981, pp. 43-62.

[28] Soliman, M. O. and Baker, A. J., "Accuracy and Convergence of a Finite Element Algorithm for Turbulent Boundary Layer, Flow," *Journal of Computer Methods in Applied Mechanics and Engineering,* Vol. 28, 1982, pp. 81-102.

[29] Hess, J. L., "Calculation of Potential Flow About Arbitrary Three-Dimensional Lifting Bodies," McDonnell-Douglas Rept. MDC J5679-01, 1972.

[30] Shafir, M. and Rubin, S. G., "The Turbulent Boundary Layer Near a Corner," *Journal of Applied Mechanics, Transactions of ASME,* Vol. 76-APM.

[31] Baker, A. J. and Orzechowski, J. A., "A Continuity-Constraint Finite Element Algorithm for Three-Dimensional Parabolic Flow Prediction," *Computers in Flow Predictions and Fluid Dynamics Experiments,* ASME, New York, 1981, pp. 103-118.